Biophysical Reports

ARTICLE

Electrically stimulated droplet injector for reduced sample consumption in serial crystallography

Mukul Sonker,[1,2] Diandra Doppler,[1,2] Ana Egatz-Gomez,[1,2] Sahba Zaare,[2,3] Mohammad T. Rabbani,[1,2] Abhik Manna,[1,2] Jorvani Cruz Villarreal,[1,2] Garrett Nelson,[3] Gihan K. Ketawala,[1,2] Konstantinos Karpos,[2,3] Roberto C. Alvarez,[2,3] Reza Nazari,[2,3] Darren Thifault,[1,2] Rebecca Jernigan,[1,2] Dominik Oberthür,[4] Huijong Han,[5] Raymond Sierra,[6] Mark S. Hunter,[6] Alexander Batyuk,[6] Christopher J. Kupitz,[6] Robert E. Sublett,[6] Frederic Poitevin,[6] Stella Lisova,[6] Valerio Mariani,[6] Alexandra Tolstikova,[4] Sebastien Boutet,[6] Marc Messerschmidt,[1,2] J. Domingo Meza-Aguilar,[1,2] Raimund Fromme,[1,2] Jose M. Martin-Garcia,[7] Sabine Botha,[2,3] Petra Fromme,[1,2] Thomas D. Grant,[8] Richard A. Kirian,[2,3] and Alexandra Ros[1,2,*]

[1]School of Molecular Sciences, Arizona State University, Tempe, Arizona; [2]Center for Applied Structural Discovery, The Biodesign Institute, Arizona State University, Tempe, Arizona; [3]Department of Physics, Arizona State University, Tempe, Arizona; [4]Center for Free-Electron Laser Science, Deutsches Elektronen-Synchrotron, Hamburg, Germany; [5]European XFEL GmbH, Schenefeld, Germany; [6]Linac Coherent Light Source (LCLS), SLAC National Accelerator Laboratory, Menlo Park, California; [7]Institute Physical-Chemistry Rocasolano, Spanish National Research Council, Madrid, Spain; and [8]Department of Structural Biology, Jacobs School of Medicine and Biomedical Sciences, SUNY University at Buffalo, Buffalo, New York

ABSTRACT With advances in X-ray free-electron lasers (XFELs), serial femtosecond crystallography (SFX) has enabled the static and dynamic structure determination for challenging proteins such as membrane protein complexes. In SFX with XFELs, the crystals are typically destroyed after interacting with a single XFEL pulse. Therefore, thousands of new crystals must be sequentially introduced into the X-ray beam to collect full data sets. Because of the serial nature of any SFX experiment, up to 99% of the sample delivered to the X-ray beam during its "off-time" between X-ray pulses is wasted due to the intrinsic pulsed nature of all current XFELs. To solve this major problem of large and often limiting sample consumption, we report on improvements of a revolutionary sample-saving method that is compatible with all current XFELs. We previously reported 3D-printed injection devices coupled with gas dynamic virtual nozzles (GDVNs) capable of generating samples containing droplets segmented by an immiscible oil phase for jetting crystal-laden droplets into the path of an XFEL. Here, we have further improved the device design by including metal electrodes inducing electrowetting effects for improved control over droplet generation frequency to stimulate the droplet release to matching the XFEL repetition rate by employing an electrical feedback mechanism. We report the improvements in this electrically triggered segmented flow approach for sample conservation in comparison with a continuous GDVN injection using the microcrystals of lysozyme and 3-deoxy-D-manno-octulosonate 8-phosphate synthase and report the segmented flow approach for sample injection applied at the Macromolecular Femtosecond Crystallography instrument at the Linear Coherent Light Source for the first time.

WHY IT MATTERS Serial crystallography of proteins with powerful X-ray lasers is an emerging field in structure determination but is hampered by the large amount of protein sample needed for relevant protein structure determination, making this approach cumbersome and cost intensive. To overcome these serious limitations, we developed a novel injector delivering protein crystal sample to the path of the X-ray laser. We encapsulate the protein crystals in droplets intersected by an immiscible oil and show that the droplet release can be electrically triggered in a tailored microfluidic droplet detector. We demonstrate this novel injection principle at the Macromolecular Femtosecond Crystallography instrument at the Linac Coherent Light Source and characterize the droplet generation quality as well as diffraction of injected protein crystals.

INTRODUCTION

Serial femtosecond crystallography (SFX) with X-ray free-electron lasers (XFELs) is a powerful technique used for the structure determination of various biomolecules, especially proteins (1–3). The advent of XFELs

Submitted August 2, 2022, and accepted for publication September 27, 2022.

*Correspondence: alexandra.ros@asu.edu

Editor: Jorg Enderlein

https://doi.org/10.1016/j.bpr.2022.100081

has been a vital milestone for the advancement of the field of SFX owing to the availability of high-energy femtosecond X-ray pulses interacting in a serial manner with protein crystals at room temperature in vacuum or helium (4–6). The short-lived, high-energy X-ray pulses are essential for obtaining diffraction information prior to the destruction of the micrometer-sized crystals, which is often referred to as the "diffract before destroy" principle (7). However, Holmes et al. (8) recently reported multi-hit SFX from a single lysozyme crystal using the MHz pulse structure of the European XFEL (EuXFEL). About a decade ago, Chapman et al. (5) reported the first SFX experiment with XFELs using the protein photosystem I, while Boutet et al. (9) demonstrated higher resolution by resolving the static structure of lysozyme using microcrystals ($\approx$3 μm) that diffracted to 1.9 Å resolution using the Coherent X-ray Imaging instrument at the Linac Coherent Light Source (LCLS) (10,11). These promising results motivated crystallographic studies of more complex proteins and paved the way for novel discoveries such as the elucidation of membrane protein structures including G-protein-coupled receptors (GPCRs) that followed shortly after (12–14). For example, Liu et al. (15) reported the 2.8-Å high-resolution structure of human serotonin receptors, and structural details of further membrane proteins have been studied and reported since then using XFELs (16–20). SFX with XFELs may also be advantageous over traditional macromolecular synchrotron X-ray crystallography due to its ability to use comparatively smaller (nano- to microscale) crystals at room temperature without the need for cryo-cooling, yet still avoiding structure-altering radiation damage (21–24).

SFX with XFELs is not only restricted to static studies but has also been widely used in time-resolved SFX (TR-SFX) experiments for studying reaction intermediates with the ultimate goal of revealing how these biomolecular entities work in detail (25,26). The method allows for studying reaction mechanisms with a millisecond or larger time resolution such as required in enzymology but also for fast light-induced reactions down to femtosecond time scales (27,28). By now, numerous biomolecular structures have been studied, elucidated, and updated with TR-SFX using the six currently operational hard X-ray XFEL facilities worldwide (29). Some reports included light-induced excitation of photoactive proteins such as photosystems I and II (30–33), the photoactive yellow protein (34–36), bacteriorhodopsin (37,38), and, more recently, phytochrome proteins (39). Another widely used method for TR-SFX is known as mix and inject serial crystallography (MISC) whereby a substrate is mixed with protein crystals directly before interacting with the XFEL beam, allowing structural changes to be studied in minutes to sub-millisecond timescales (40,41). MISC typically involves mixing substrate and protein crystals using a fluidic junction and then injecting the mixture into the path of the X-ray beam as a jet using a downstream gas dynamic virtual nozzle (GDVN), one of the most common injection techniques used to deliver crystals to the XFEL beam (42–44). The timescale between the mixing of crystals and the interaction with the X-ray pulse determines the timescale for structural changes that can be observed.

In recent years, novel adaptations for MISC sample delivery targeting short timescales (sub-milliseconds) (45–47) have been developed using double flow-focusing nozzles (DFFN) (48) and hydrodynamic focusing (49) based on continuous sample delivery methods (50). Despite the new structural discoveries achieved with these methods, resolving structural changes using TR-SFX still poses several challenges. One of the most limiting bottlenecks is the amount of protein required to obtain a complete data set. Since each crystal is exposed only once in an unknown position and orientation, a large number of diffraction patterns is required to account for stochastic variations in crystal quality and other factors that affect the structure factor determination. Because all current operational XFEL facilities are pulsed ranging from 10 Hz pulse trains at the EuXFEL with MHz repetition rates within the pulse train (51) to 120 Hz pulses at the LCLS (11) and projected repetition rate of up to 1 MHz at LCLS-II, which is planned for first user operation in the fall of 2022, a majority of the injected sample never interacts with the X-rays. For example, the volume fraction of a 40 m/s liquid jet that is exposed to a 1-μm X-ray beam at 120 Hz repetition rate is only 3×10^{-6}. Thus, sample consumption with continuous liquid jets is one of the major bottlenecks of the field requiring up to gram(s) of crystallized protein for obtaining a complete data set. This immense sample consumption need is even magnified in TR-SFX with MISC, where the required amount of protein is multiplied by each time point studied.

To overcome the sample consumption challenges, several sample conservation strategies for delivering crystals have been reported in the past years. Fortunately, smaller crystal size requirements and the ability to deliver crystals at room temperature have opened the door to new sample delivery methods for XFEL-based crystallography (52). Delivery of crystals on solid supports, also known as "fixed targets," is one of the approaches whereby sample crystals are loaded on a matrix or a support device made from highly X-ray transparent materials such as silicon chips (53,54), thin membranes (55,56), elastomers (57), and thermoplastic materials (58,59), enabling in some cases more than 100% hit rates (multiple crystals per shot) as opposed to the typically low hit rates (1%–10%) currently

achievable with continuous liquid delivery systems (6,60–62). Recently, Shelby et al. (63) reported a combined polymer thin film and graphene-based device for fixed-target applications in vacuum. Lee et al. (64) developed an array of polyimide tubes containing proteinase K microcrystals in a viscous medium as a fixed target and reported its crystal structure at 1.85 Å resolution. Despite the high sample hit rate, fixed-target devices usually require crystal reloading with a new chip, which can be a time-intensive procedure during allocated beamtimes (particularly for data collection in vacuum). Furthermore, evaporation during data collection as well as target mounting is a challenge for many fixed-target applications, and MHz repetition frequencies can hardly be achieved. Also, these devices have difficulty in accommodating crystals in a lipidic environment required for the crystallization of membrane proteins with high medical relevance, especially GPCRs. To overcome such challenges, low-flow-rate injectors containing highly viscous media including, but not restricted to, the lipidic cubic phase (LCP) (65,66) have been developed to deliver membrane protein crystals in their near-native lipidic environment (67,68). Applying a similar principle of decreased flow rate in continuous liquid injection for sample conservation was also developed, employing a hybrid electrokinetic technique called microfluidic electrokinetic sample holder (MESH) (69), which further evolved to a mixing injector named concentric MESH (70). In this method, a potential of up to 5000 V is applied across an open capillary with small flow rates offering reduced sample consumption. Since an open capillary is used to electrospin the crystal slurry into the path of the X-ray beam, the liquid volume surrounding the crystals is larger compared with a thin liquid jet, exhibiting higher background and imposing challenges to data analysis. Additionally, the electrical potentials may damage the crystals or alter the protein molecules' conformation, and sheathing liquids such as glycerol used with injection buffers may not be compatible with all protein crystals (71).

To reduce sample waste between XFEL pulses, segmented flow or droplet-based injection methods have been recently developed. Aqueous sample droplets are segmented with an immiscible oil phase using specialized microfluidic geometries (72,73) or generated via piezoelectric (74) or acoustic effects (75). The latter two are also referred to as droplet-on-demand techniques (76), designed and developed to generate droplets to match the pulse structures of current XFELs (52). However, drop-on-demand techniques are inherently limited by clogging effects through settling crystals and are incompatible with vacuum conditions. To overcome limitations with drop-on-demand techniques, we previously developed a three-dimensional (3D)-printed device capable of generating and electrically stimulating droplets segmented by an immiscible oil phase. The device creates crystal-laden droplets and allows injection with a downstream GDVN (43). We demonstrated the successful segmented droplet sample injection for SFX with XFELs (73,77) and obtained the room-temperature structure of the 3-deoxy-D-manno-octulosonate 8-phosphate synthase (KDO8PS) protein with this droplet injection method at the EuXFEL (51). To further stimulate the droplet release with the ultimate goal of synchronizing the droplet arrival at the interaction region with the XFEL pulses, we recently demonstrated that electrowetting effects can be employed to tune the droplet generation frequency and phase (72).

Here, we further develop this approach and demonstrate SFX with stimulated droplet injection for the first time at the LCLS. We show the adaptation of this droplet injection method to the 120 Hz of the LCLS XFEL repetition frequency and explore an electrical feedback mechanism for adjusting the droplet generation frequency and delay relative to the XFEL reference. Capillary coupled 3D-printed droplet injection devices (CCDIDs) for sample delivery along with data monitoring of the droplet frequency were implemented at the Macromolecular Femtosecond Crystallography (MFX) instrument (78,79) while delivering KDO8PS and lysozyme microcrystals into the X-ray beam. We demonstrate the long-term injection of droplets containing either of these two proteins and characterize the electrical feedback mechanism as well as the CCDIDs in detail.

MATERIALS AND METHODS

Chemicals and materials

Glass slides (76 × 25 × 1 mm) were purchased from Fisher Scientific (Pittsburgh, PA). Perfluorodecalin (PFD), 1H,1H,2H,2H-perfluoro-1-octanol (PFO), hen egg-white lysozyme (HEWL), Tris-base, HCl, KCl, NaCl, poly(ethylene glycol) methyl ether 550 (PEGME 550), poly(ethylene glycol) (PEG) 3350, and PEG 4000 were purchased from Sigma-Aldrich (St. Louis, MO). SU-8 developer was obtained from Kayaku Advanced Materials (Westborough, MA). The photoresist IP-S was purchased from Nanoscribe (Eggenstein-Leopoldshafen, Germany). Deionized water (18 MΩ) was supplied from a LA755 Elga purification system (ElgaLab Water, Woodridge, IL), and isopropyl alcohol (IPA) was obtained from VWR Analytical, (Radnor, PA). Novec 1720 electronic grade was generously provided by 3M (St. Paul, MN). Fused silica capillaries (360 μm outer diameter [OD], 100 μm inner diameter [ID]) were purchased from Molex (Lisle, IL). Extra-fast setting epoxy was purchased from Hardman (Wilmington, CA). Various fluidic unions and connectors for capillaries were purchased from IDEX Health and Sciences (Carlsbad, CA). PEEK tubing was purchased from Zeus (Orangeburg, SC). Zirconia ferrules for home-made optical fibers were purchased from OZ Optics (Ottawa, ON, Canada). Single-mode fiber (125 μm core and 900 μm OD) connectors and thermal epoxy (353NDPK) were purchased from Thorlabs (Newton, NJ). Multimode optical fiber (125 μm core and 900 μm OD) connectors were purchased from Markertek (Saugerties, NY).

Protein crystals and oil phase preparation

HEWL crystals were prepared as described previously (22,80). In brief, crystals between 5 and 10 μm in size were prepared by the rapid-mixing batch method by adding three parts of precipitant (1 M NaCl, 40% [v/v] ethylene glycol, 15% [w/v] PEG 4000, 50 mM acetate buffer [pH 3.5]) to one part of HEWL (126 mg/mL; Sigma-Aldrich). After vortexing, this solution was incubated for 30 min to allow crystal growth and then optically analyzed for size and uniformity using a stereomicroscope. Finally, the rod-shaped crystals were resuspended in different injection/wash buffers before injection to make a homogeneous suspension and reduce the precipitant concentration to avoid clogging. These crystals were washed and suspended in 0.025 M sodium acetate (pH 3.5) (8% [w/v] NaCl) to make the initial lysozyme crystal sample (L1). Two more lysozyme samples of different viscosities were also prepared by adding 20% PEG 3350 (L2) or 20% PEGME 550 (L3) to L1 (Table 1). The various buffer viscosities (reported in Table S1) were measured using a modular compact rheometer (MCR 92; Anton Paar USA, Ashland, VA) in the XBI Biolab at the EuXFEL (Schenefeld, Germany) ($n = 40$ for each sample) (81).

The wild-type KDO8PS genes (GenBank accession number NC-0000913) were purchased from GenScript (Piscataway, NJ) as a synthetic gene in the pET-23d plasmid. The protein expression and purification were carried out as reported previously (51,82). The KDO8PS crystallization was performed by a batch method with seeding. First the seeds were prepared as follows: 450 μL of 30% PEG 3350 in 0.1 M Tris-HCl (pH 8.0) was added to 150 μL of KDO8PS (20 mg/mL), and the suspension was vigorously mixed by pipetting the suspension 50 times up and down. The sample was then incubated for 20 min at room temperature. The crystals for the delivery to the XFEL were then grown using the following procedure: 560 μL of the seeds was added to 2.1 mL of precipitant (30% PEG 550, 0.1 M Tris-HCl [pH 8.0]). The precipitant with the seeds was then added quickly to 350 μL of KDO8PS protein (20 mg/mL) in a 15 mL Falcon tube, then stored at 4°C for 4 h. After imaging of the crystals under a stereomicroscope, the crystal suspension was further concentrated to reach a higher crystal density. However, the crystal density was generally very low (approximately 10^4 crystals/mL). The crystal suspension was divided into three portions and centrifuged in 1.5-mL reaction vessels at 4°C for 4 min at 800 rpm, after which 750 μL of the supernatant was removed from each of the reaction vessels and the crystals resuspended in the remaining solution. This sample was then filtered through a 30-μm mesh filter. To fully recover all crystals, the filter was washed with 200 μL of the removed supernatant, and the wash solution was combined with the concentrated crystal sample for a final volume of 2.4 mL at a crystal density of approximately 2×10^4 crystals/mL. The crystal suspension was stored at 4°C until it was loaded into the 4°C cooled reservoir mounted on the anti-settling device for sample delivery.

The immiscible oil phase was prepared by mixing PFD and PFO at a 10:1 ratio, respectively. This mixture was then filtered using a 0.2-μm syringe filter (Fisher Scientific) and degassed with helium for 20 min before loading it into the stainless-steel reservoir for experiments.

Capillary coupled injector device design and fabrication

All components of the device were designed and fabricated as previously described (51,72,73). In brief, the devices were designed in Fusion 360 (Autodesk, San Francisco, CA), and 3D printed with a Photonic Professional GT 3D printer (Nanoscribe) using the proprietary IP-S photoresist. Printed devices were developed in SU-8 developer and rinsed in IPA. The complete CCDID consisted of three components, as shown in Fig. 1. The first component was a Y-shaped droplet generator with two (100 × 100 μm) rectangular fluidic channels joined at an angle of 45°. This droplet generator also contained two rectangular electrode channels (350 × 100 × 50 μm^3) situated parallel to the continuous channel along the droplet generating region. These electrode channels were filled with conductive epoxy (MG Chemicals, Burlington, ON, Canada) and connected via two nickel-chrome wires to serve as electrodes. The wires were further extended to 2 m each with an insulated copper wire (Remington Industries, Johnsburg, IL) so that electrical connections could be made outside of the helium-rich ambient (HERA) chamber. The second component was an optical fiber-capillary aligner for the optical detection of droplets, described in detail in "optical droplet detection and electrical feedback." The third component was a 3D-printed GDVN (43,83) for creating a sample jet.

Fluid supply lines for oils and sample were accomplished through two 1.5-m silica capillaries (360 μm OD, 100 μm ID) glued to the aqueous and oil inlets of the droplet generator, respectively. Another shorter piece of the capillary was then inserted and permanently glued to the droplet generator outlet. The outlet capillary was threaded through the droplet detector holder as shown in Fig. 1, *B* and *C* and further described in "optical droplet detection and electrical feedback." The end of the outlet capillary was then connected and glued to a 3D-printed GDVN to generate a sample jet from the segmented oil-sample fluid. The end of another 1.5-m capillary was glued to the gas inlet of the GDVN for delivering He at 200–350 psi. The inner fluid capillaries of the completely assembled device were then treated with Novec 1720 to create a hydrophobic surface on channel walls essential for droplet generation, as previously described (51,72,73).

Fluidic operation and setup

Oil and crystal samples were supplied through stainless-steel reservoirs (custom-made and supplied by LCLS) pressurized by HPLC pumps (LC20AD; Shimadzu, Kyoto, Japan). PEEK tubing (Zeus, 100–250 μm ID and 1.6 mm OD) along with fittings and ferrules (IDEX Health and Sciences) were used to connect the oil and sample reservoirs with the pumps. To avoid settling of the suspended protein crystals, the reservoirs were mounted on a scaled-down version of the anti-settling shaking instrument previously reported by Lomb et al. (84). Fused silica capillaries connected to reservoirs allowed transport of the crystal sample and oil phase into the droplet generator at typical flow rates of 15–22 μL/min and 3–8 μL/min for oil and sample, respectively. A photograph of the actual experimental setup deployed during the LV14 experiment at LCLS at the MFX instrument is shown in Fig. S2 *A*. Devices were mounted on a custom bracket in the HERA chamber (79). The capillaries, optical detector fibers, and insulated wires were fed through ports on the side walls of the chamber as shown in a photograph in Fig. S2 *B*. The helium pressure to create the jet exiting the 3D-printed GDVN was regulated by a high-pressure gas valve (Proportion-air, McCordsville, IN) to produce stable liquid jets.

Optical droplet detection and electrical feedback

Differences in the refractive index and optical absorption at 1470 nm between oil and aqueous samples were used to monitor the droplets in a custom setup. A 1470 nm, 5 mW, single-mode (SM), SC/FC terminated pigtailed laser diode (Qphotonics, Ann Arbor, MI) was used for excitation, and a home-made SM optical fiber patch (EZ-Bend; OFS, Norcross, GA) terminated with a custom zirconia ferrule (1 mm OD, 126 μm ID; OZ Optics) was used to transversely illuminate the fused silica capillary carrying the droplets from the droplet generator to the GDVN. Another home-made custom multimode optical fiber (OM4; Corning, Corning, NY) patch terminated with another zirconia ferrule was used to collect the light passing through the fused silica capillary into a 5-GHz InGaAs

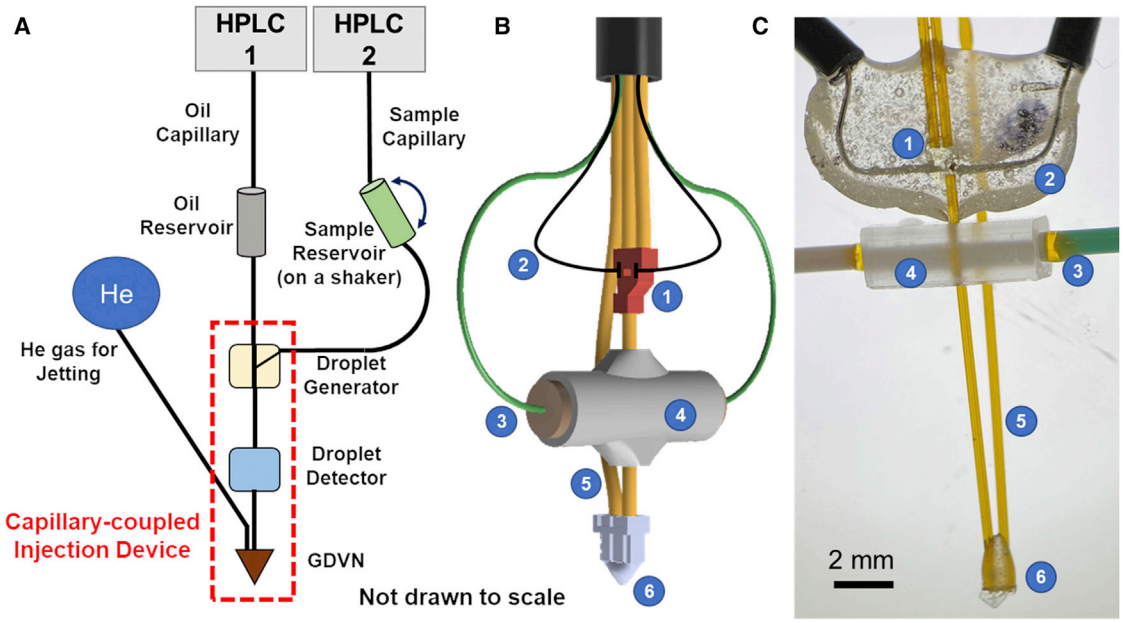

FIGURE 1 Schematic of the droplet injection setup and injector assembly details. (*A*) Representation of the elements required for droplet injection. (*B*) Representation of the capillary coupled droplet injector device consisting of 1) the 3D-printed droplet generator, 2) electrodes, 3) optical fibers, 4) fiber-capillary aligner device, 5) He gas supply line, and 6) 3D-printed GDVN. (*C*) Photograph of a completely assembled device showing the same elements as the schematics in (*B*).

photodiode detector (DET08CFC; Thorlabs). A fiber-capillary aligner device was used to position the center of the capillary in the optical path between the two optical fiber cores. The aligner was initially built using a commercially available brass sleeve (courtesy of Daniel Tsue, Senko, CA) with a 0.8-mm home-made through-hole as well as a 3D-printed ring to center the capillary and the ferrules (Fig. S1 *B*). The second aligner version consisted of a custom completely 3D-printed design (Figs. 1 *C* and S1 *C*) from Acrea 3D (Herriman, UT). The photodetector signal was continuously recorded using LabChart 8 software (AD Instruments, Colorado Springs, CO) via a PowerLab instrument (PL3508; AD Instruments). This droplet signal was also recorded using a Raspberry Pi (Model B; Raspberry Pi Foundation, Cambridge, UK) equipped with a microprocessor (MCC 118; Digilent, Pullman, WA). A digital delay generator (DG645; Stanford Research Systems, Sunnyvale, CA) and a high-voltage amplifier (Model 2210; Trek, Lockport, NY) were used to apply a short, millisecond-long DC voltage pulse for droplet stimulation. Custom Python scripts (85) were employed to diagnose the droplet generation frequency and phase based on the photodetector traces, which were triggered by the XFEL reference pulse. A custom algorithm was developed to periodically adjust the delay of the electrical stimulus relative to the XFEL reference based on the recent history of recorded droplet leading-edge positions. Updates to the electrical stimulus delay were typically implemented once per second, i.e., once per 120 XFEL pulses. All electrical components were connected with BNC cables. For XFEL experiments during the LW79 beamtime, a custom attenuator made of resistors on a breadboard with BNC connectors was used to decrease the output voltage of the photodetector before feeding into an Acqiris DC282 10-bit Digitizer (Artisan Technology Group, Champaign, IL) for direct recording of the droplet signal through the MFX Experimental Physics and Industrial Control System (Epics) at SLAC.

Diffraction experiments

Serial femtosecond crystallography experiments on microcrystals of lysozyme and the KDO8PS proteins were conducted at the MFX instrument at LCLS during beam times LV14 and LW79. During LV14, 40-fs pulses with an average pulse energy of 0.67 mJ were delivered at 120 Hz at 8.75 keV photon energy. During LW79 experiments, 40-fs pulses with an average pulse energy of 0.4 mJ were delivered at 120 Hz at 9.5 keV photon energy. The X-ray spot size was 3–5 μm, and the diffraction patterns were collected on the ePix10K-2.2M detector (operated in the automated low-medium gain switch) for both experiments. Data analysis protocols including Cheetah (86) and OM (87) for high-throughput data reduction, peak finding, detector artifact removal, and live feedback of hit rates and data quality, as well as CrystFEL (88) for auto-indexing, merging, and scaling the single-shot diffraction patterns, were employed. A "hit" was classified to have a minimum of 8 peaks above a threshold of 150, a signal/noise ratio of 4.0, and at least 1 pixel contributing to the peak (as defined in Peakfinder 8). Indexing was performed with CrystFEL 0.10.1 using the indexing algorithms XGANDALF (89), iMosflm (90), and DIRAX (91), allowing for multiple lattices to be indexed in a single image. Furthermore, a custom X-ray scattering-based droplet detection analysis approach integrated with the OM live feedback software (87) was used to assess the interaction of the X-ray beam with the droplets. Droplet hits were identified from X-ray images using one-dimensional radial scattering profiles where the ratio of the water scattering peak to the oil scattering peak was greater than a threshold of 0.5, indicating significant water scattering. Droplet hit rates were then calculated as the number of droplet hits per hundred frames.

RESULTS AND DISCUSSION

Droplet injector design

In previous work, we demonstrated the ability to solve the structure of the enzyme KDO8PS when crystals were injected in droplets segmented with an immiscible

oil phase (51). Here, we demonstrate an electrical stimulation feedback mechanism that allows adjustment of the droplet generation frequency to match a particular XFEL pulse profile, which will be demonstrated with the 120 Hz corresponding to the repetition rate of the LCLS XFEL (11). Since each XFEL end station and experimental chamber present different physical configurations, we describe an adapted experimental setup and devices to comply with the requirements of the MFX instrument (78) and the HERA chamber (79) for injection of lysozyme and KDO8PS crystal-laden droplets with electrical droplet stimulation.

Droplet generation was accomplished with the experimental setup shown in Fig. 1 *A*. Both sample and oil were loaded in a steel reservoir and delivered via high-pressure pumps into the HERA chamber. The droplets were generated with a CCDID that consisted of three main elements as shown in Fig. 1 *A*: 1) the droplet generator with integrated electrodes for stimulation; 2) an optical fiber droplet detector; and 3) a GDVN for generating the sample jet. The CCDID schematic and a photograph of the assembled device are shown in Fig. 1, *B* and *C*. A major upgrade to our previously published segmented flow injector is a smaller footprint of the droplet detector allowing the entire device to be installed in a vacuum or helium chamber for SFX experiments. The home-made fiber cables, consisting of ferrules on a bendable fiber end, allow the fully assembled injector width to be less than 32 mm. This is advantageous for insertion into serial crystallography experimental chambers, where injector space is typically restricted. These upgraded devices were robust and could be reliably and reproducibly installed in the HERA chamber at MFX at LCLS.

Characterization of droplet generation and electrical feedback mechanism

A 3D-printed intersection of two microfluidic channels was used to create a segmented flow forming aqueous droplets separated by fluorinated oil. In contrast to our previous work, the hydrophobic coating on the channel walls employed here promotes the formation of sample-in-oil droplets instead of a "co-flow" of the two immiscible liquids downstream of the Y-intersection (92). The droplet generation frequency can be controlled with the oil and aqueous flow rates as well as the geometry of the intersecting microfluidic channels in the droplet generator (51). To improve droplet generation reproducibility and avoid potential clogging effects with crystal-laden droplets, we further changed the angle at which the two microfluidic channels intersect to 45° as compared with 90° in the previous work (51). The electrical stimulation of the droplets was achieved through integrated electrodes in close proximity to the Y-intersection. We exploited the advantages of 3D printing for the fabrication of these microelectrodes by integrating two additional parallel channels filled with conductive material, as shown in Fig. 2 *A*. Additional detailed design schematics of the 3D-printed droplet generator and micrographs are provided in Fig. S1 *A*. Fig. 2, *B* and *C* show snapshots of droplets generated with KDO8PS crystals supplied through the sample inlet and oil through the continuous (straight) channel inlet. During injection without electrical stimulation, the droplets are sheared off the inlet section of the sample channel at the intersection of the two channels and are carried downstream segmented by the oil. When an electrical stimulus is provided as a short (millisecond) voltage pulse, the droplets are pulled toward the channel wall opposite to the aqueous channel by an electrowetting effect (72). There are two main consequences of the applied voltage pulse. First, since the droplet is very briefly held at the walls near the channel intersection, a time delay in droplet release is induced. Second, when a sequence of electrical pulses at a given frequency is applied, the droplets will be generated at the same frequency, which allows for the fine-tuning of the droplet frequency to match that of the XFEL.

The electrical feedback mechanism was set up as schematically shown in Fig. 3 *A*. Owing to the CCDID manual assembly procedure including a short intersecting capillary piece, the droplets are generated about 15–20 mm upstream of the GDVN nozzle; therefore, the location of the droplet generator varied by about 5 mm along the distance from droplet generator to nozzle. The droplet detection principle is based on refractive index and absorption differences between the aqueous and oil phase at the 1470-nm excitation wavelength and the capillary and droplet curvature. The corresponding voltage changes induced at the photodiode of the droplet detector assembly and the XFEL reference signal were recorded as described in materials and methods. A custom Python script detected the leading edge of the droplet signal, compared it with the XFEL reference signal, and calculated the time delay of the trigger event compared with that of the reference. When operating in feedback modus, the algorithm adjusted the applied electrical DC signal in phase relative to the XFEL reference to optimize droplet synchronization. The script also allowed the adjustment of the amplitude and duration of the electrical pulse applied to the droplet generator to optimize droplet generation for each CCDID and employed sample. This functionality of the feedback mechanism is essential to account for the adjustments in the time difference of the triggering event to the XFEL reference, which is caused by the geometric variations

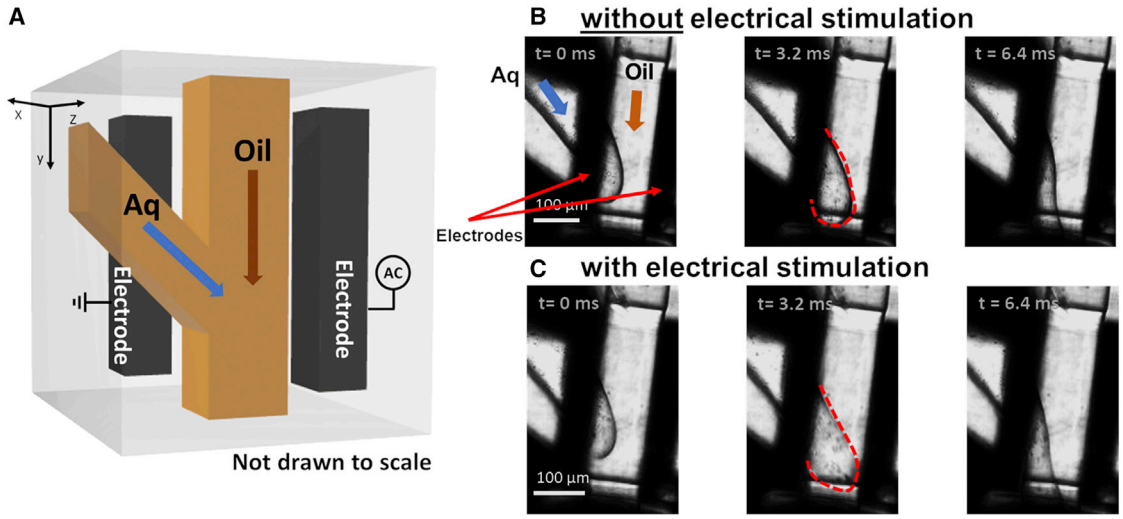

FIGURE 2 Droplet generator design and electrical stimulation
(*A*) Schematic of the 3D-printed droplet generator showing the Y-intersection of flow channels (*yellow*) for oil and sample as well as electrodes (*dark gray*) for electrical stimulation. (*B*) Image snapshots of droplet generation at 120 Hz with KDO8PS crystal-laden buffer without electrical stimulation. (*C*) Image snapshots of droplet generation at 120 Hz with the same sample as in (*B*) but with electrical stimulation. Electrical pulses of 200 V amplitude and 2 ms duration were employed. The wetting effect of the buffer solution on the inner channel wall is apparent at 3.2 ms as indicated by the red dashed line. This effect causes the ability to adjust frequency and delay in reference to XFEL pulses. The dark speckles in the sample droplet in (*B*) and (*C*) are the KDO8PS crystals in solution.

of the droplet generation system. The amplitude of the electrical pulse varied from 100 V to 350 V, and the time delay could be adjusted within one period of the XFEL repetition rate (8.3 ms). Fig. 3 *B* exemplarily shows recorded traces for the XFEL reference, detected droplet signal, trigger events, and the resulting droplet generation frequency observed for lysozyme crystal-laden droplets triggered at 250 V to

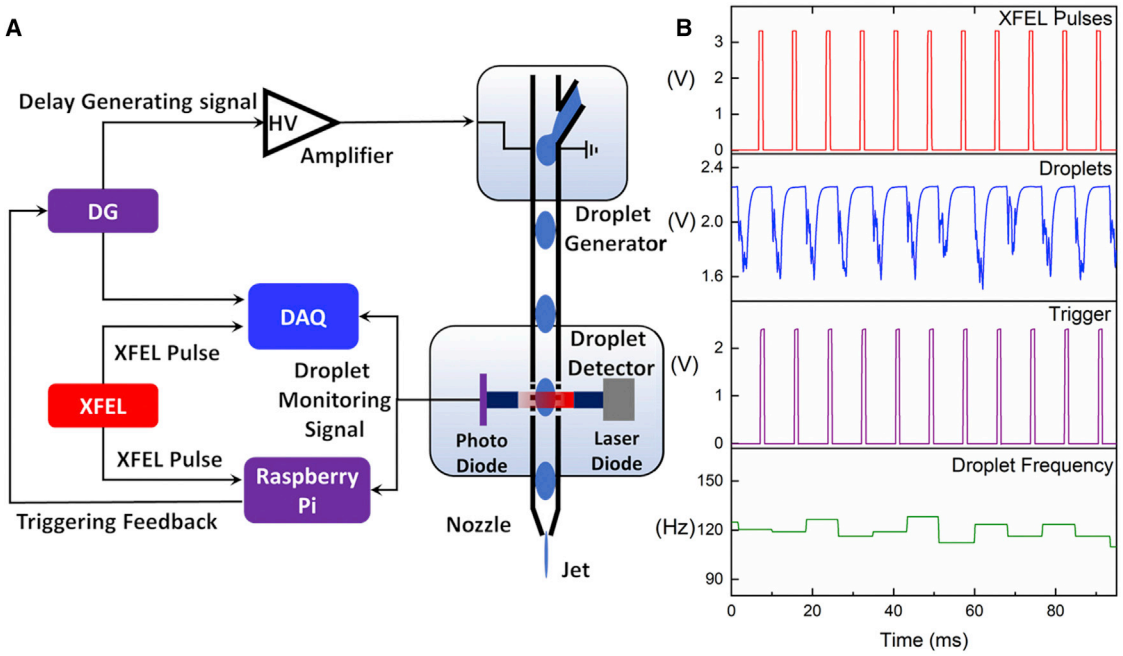

FIGURE 3 Electrical feedback and data aquisition
(*A*) Schematic of the experimental setup and instrumentation for the electric feedback mechanism deployed for continuous triggering at a given frequency and delay to the XFEL pulse. (*B*) Selected plots of real-time data stream recorded for XFEL reference (*red*), droplet detector (*blue*), electrical trigger (*purple*), and resultant droplet frequency (*green*) during the LV14 beamtime.

maintain 120 Hz droplet frequency with the CCDID operating at the MFX instrument.

The feedback mechanism was first tested during continuous droplet injection at the MFX instrument in the HERA chamber during beamtime LV14 to characterize the custom droplet injection setup (see Fig. S2 for detailed images) with injection buffer not containing crystals. Fig. 4 *A* (*top*) demonstrates the droplet injection as recorded without electrical stimulation and the corresponding XFEL reference for a period of 40 ms. A useful visual representation of continuous injection over several seconds is depicted in Fig. 4 *A* (*bottom*) in a waterfall plot, where each horizontal line corresponds to a heatmap of the droplet detector signal within one XFEL period. The waterfall plots in the bottom panels shown in Fig. 4 comprise 1000 stacked droplet traces while 4–5 droplets are shown in the top panels. Without electrical stimulation, the droplet frequency fluctuated considerably with respect to the XFEL pulses, and the droplet generation frequency was below 120 Hz (Fig. 4 *A*). In contrast, when the feedback mechanism was activated, the droplets were generated with a defined delay with respect to the XFEL reference at 120 Hz. Fig. 4, *B* and *C* demonstrate programmed delays of 2 ms and 7 ms, respectively. The droplets align well, and the leading edge of the droplet corresponds to the programmed time delay within an error of approximately <0.5 ms. This example with lysozyme injection buffer demonstrates the successful working principle of the feedback mechanism.

Next, we tested the droplet injection with the feedback mechanism for crystal suspensions. The droplet trace analysis revealed that the content of crystals in the droplets was reflected in the droplet detector signal. When crystals were present in the aqueous droplet, this variation mainly occurred as fluctuations of the traced minima and is due to variation in refraction and absorption effects of the excitation light caused by the protein crystals present in the droplets. This becomes evident when comparing the droplet detector trace of Fig. 5 *A* (*top*) with Fig. 4 *A* (*top*). The distorted portion of the droplet trace following the leading edge is a clear indication of crystals being present in the droplets and could be used to diagnose crystal incorporation into the sample phase droplets. In addition, we note that variations in the manual assembly of the droplet detector and the optical properties of

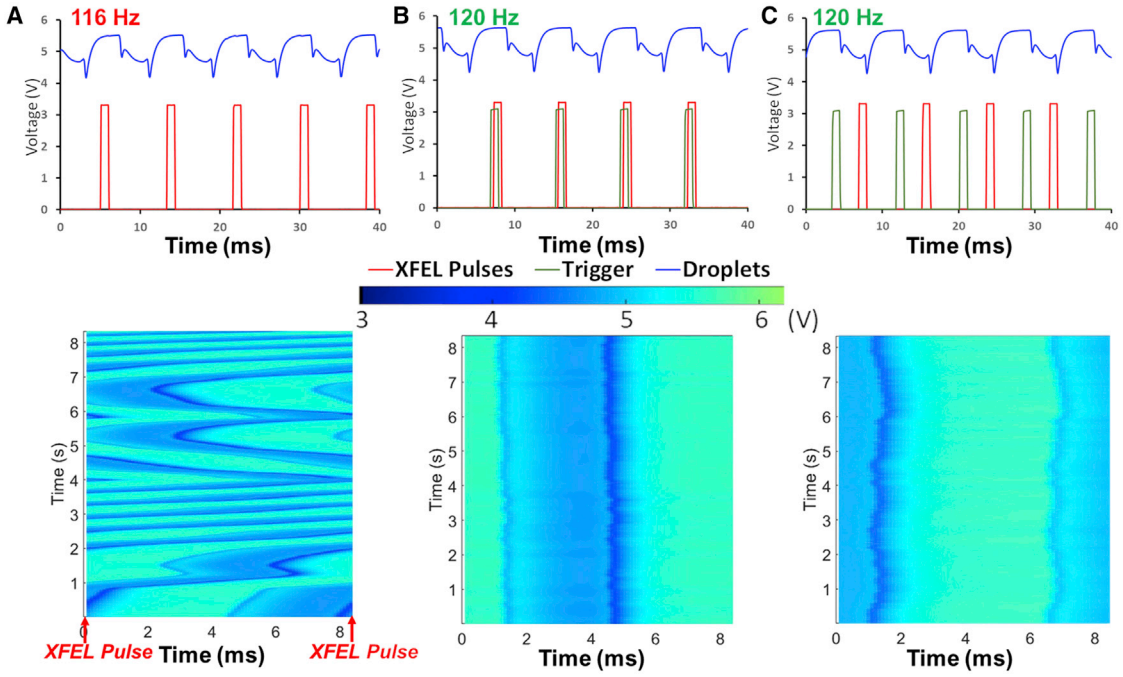

FIGURE 4 Representation of XFEL signal (*red*), droplet signal (*blue*) as recorded by the droplet detector, and electrical stimulus (*green*) (*top*) and resulting waterfall plots (*bottom*). (*A*) Frequency variation is apparent when droplets were generated based on flow-rate ratio differences between oil and aqueous phase alone without electrical stimulation. Top: the depicted time interval of $\approx$40 ms shows droplets generated at a frequency of 116 Hz, slightly lower than the required 120 Hz. Bottom: the waterfall plot shows frequency variation patterns over a larger 8 s period. (*B* and *C*) Stimulated droplet generation frequency with active feedback aiming for a programmed delay of (*B*) 2 ms and (*C*) 7 ms to the XFEL reference signal. Lysozyme injection buffer (L2) served as the sample in (*A*)–(*C*). The color scale represents the voltage signal recorded with the photodetector (in volts). The feedback mechanism "pins" the droplet leading-edge position at the desired delay to the XFEL reference in (*B*) and (*C*) successfully. Note that the droplet appears wrapped around the XFEL reference in the waterfall plot in (*C*), since the droplet leading edge is successfully programmed to 7 ms, but the droplet width is $>$2 ms.

the sample buffer could cause variations in the overall shape of the droplet trace. One example of the variation between optical detector assemblies is demonstrated in Fig. 5, *A* and *B* (*top panels*). In Fig. 5 *A* the presence of sample droplets is apparent as voltage reduction, whereas in Fig. 5 *B* a voltage maximum in the middle of the droplet occurred. Such pronounced variations, however, did not lead to significant issues in detecting the droplet leading edge and did not hinder the employed algorithm.

We next assessed the long-term stability of crystal sample droplet generation with the feedback mechanism. Fig. 5 demonstrates waterfall plots for extended periods (over 200,000 droplets each) where lysozyme (Fig. 5 *A*) and KDO8PS (Fig. 5 *B*) crystal-laden droplets were injected. In addition to the color representing the intensity of the droplet signal, the duration of the electrical stimulus via the integrated electrodes in the droplet generator is depicted in white. As apparent in Fig. 5 *A* (*bottom*), continuous droplet injection at 120 Hz was achieved upon the application of a fixed delay of 7.5 ms for the first 10 min. However, the leading edge of the droplet varied from 0 to 3 ms. To minimize this variation, the feedback mechanism was turned on to actively adjust the delay to 7.5 ms. As a result, the droplet leading edges were detected at 7.5 ms with a variation of ≈1 ms for about 5 min. Note that the droplets "wrap around" the 8.3 ms mark, such that the first portion of the droplet from 7.5 to 8.3 ms appears in one horizontal line, whereas the remainder of the droplet signal shows up in the subsequent line on the waterfall plot representation. For the following 15 min (Fig. 5 *A*, *bottom*), the delay was set to 4 ms. We observe that the feedback mechanism successfully generated droplets for this programmed delay for ≈20 min. Overall, the waterfall plot in Fig. 5 *A* shows stable droplet generation at 120 Hz with a desired phase lag to the XFEL pulses over 30 min with lysozyme crystal slurry as the sample. It is also apparent that the electrical feedback mechanism improved the alignment of the droplet leading edges to the desired delay as compared with only a constant delay without active feedback (as demonstrated in the first 10 min). This constitutes an improvement of our previously developed electrical droplet stimulation, as an active feedback can now be achieved as well as the capability of electrical stimulation with direct current voltage pulses (72).

Furthermore, the droplet generation with KDO8PS crystals as depicted in Fig. 5 *B* shows results similar to those obtained for lysozyme crystal injection with stimulated droplets. The waterfall plots in Fig. 5 *B* (*bottom*) show stable droplet injection for about 25 min with the electrical feedback mechanism acting. The delay was first programmed to 7 ms and then to 1.5 ms. During the times when the 7-ms delay was activated, the electrical feedback was turned off around minute 5 and a sudden loss of temporal droplet alignment

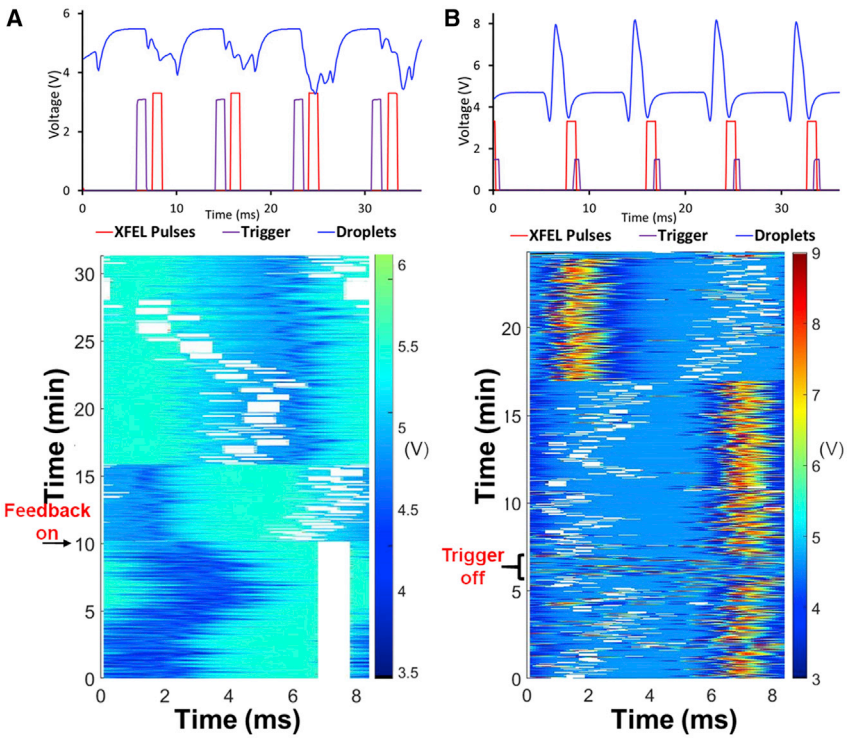

FIGURE 5 Representative data traces showing continuous droplet generation with electrical feedback mechanism as achieved in the HERA chamber: (*A*) Representation of XFEL reference signal, applied voltage pulse (trigger), and droplet signal (*top*) and resultant waterfall plot (*bottom*) for droplets generated at 120 Hz. The sample generating aqueous-phase droplets contained lysozyme crystals. (*B*) Representation of XFEL reference, applied voltage pulse (trigger), and droplet signal (*top*), and resultant waterfall plot (*bottom*) for continuously triggered droplets at 120 Hz. The sample generating aqueous droplets contained KDO8PS crystals. The duration of the trigger events and their delay to the XFEL reference are depicted by white bars in the waterfall plots. The colors in (*A*) and (*B*) correspond to the droplet detector signal measured in volts. Note the different "shape" of the droplet trace in (*B*), such that the heat plot shows voltages up to 9 V.

TABLE 1 Sample consumption and hit rate comparison of segmented injection with CCDID and continuous injection (GDVN) performed at the MFX instrument with lysozyme crystal injection in three different injection buffers

Sample	Injection method	Time (min)	Avg. flow rate (μL/min)	Total volume (mL)	Crystal hits	Crystal lattices	Indexed patterns	Lattices/ min	Hits/ min	Lattices/ μL	Hits/ μL	Resolution (Å)
L1	GDVN	21.2	23.0	0.51	1473	535	421	25.2	69.5	1.05	2.89	2.1
	droplets	76.5	4.5	0.35	1742	1311	1069	17.1	22.8	3.75	4.98	1.8
L2	GDVN	42.0	20.0	0.85	8646	6540	4980	155.7	205.9	7.69	10.17	1.8
	droplets	71.2	4.1	0.26	1904	1364	1121	19.2	26.7	5.24	7.32	2.0
L3	GDVN	51.7	20.0	1.01	2202	2760	2078	53.4	42.6	2.75	2.18	2.0
	droplets	227.7	5.1	1.20	2048	2591	1803	11.3	9.00	2.16	1.71	1.8

L1: 8% NaCl (w/v), 200 mM sodium acetate (pH 3.5); L2: 25 mM sodium acetate (pH 3.5), 8% (w/v) NaCl, 20% PEG 3350; L3: 200 mM sodium acetate, 8% NaCl (w/v), 20% PEGME 550.

became apparent. When the feedback was turned on again after ≈1 min, an immediate droplet alignment could be observed in the waterfall plot. After 17 min the delay was set to 1.5 ms, which also resulted in an immediate shift of the droplet phase. These results strongly suggest that electric triggering aids in reproducibly generating droplets with a given frequency and phase delay to the XFEL reference. We also conclude that the active feedback mechanism is suitable to reliably adjust the delay of the droplet with respect to the XFEL reference and allows stable injection over periods of ≈30 min in the HERA chamber of the MFX instrument.

Comparison of droplet injection with continuous GDVN injection

During two MFX beam times (LV14 and LW79), droplet injection by electrical stimulation was implemented and tested for various crystal samples with the CCDIDs and compared with traditional GDVN injection with the same nozzle geometry. Table 1 summarizes the duration, volume consumption, and hit rate observed for lysozyme crystals when injected in segmented flow using a CCDID or continuously using a GDVN alone. Three different buffers were used to suspend lysozyme crystals for injection. While droplet generation and electrical stimulation could be achieved over 6–12 h per beamtime shift, this table only summarizes conditions under which diffraction data were obtained with the lysozyme crystals for continuous and droplet injection. The major conclusions drawn from Table 1 are the following.

1) For lysozyme crystals, three different sample buffers could be employed varying injection buffer composition and viscosity. Stimulated droplet generation was possible with all three of them in the CCDID, and the viscosities varied between 1.3 and 8.3 m Pa s (see Table S1).
2) The crystal hit rates and indexed patterns obtained per injected volume for both injection methods were comparable, and a general increase in hit rates with increased sample viscosity (L2 and L3) was observed for both injection methods where GDVN injection exhibited slightly higher hit rates. This is also reflected in the ratio of crystal lattices observed per time and the volume ratio of this quantity. In the case of L1, the number of lattices per volume was found to be almost a factor of four higher for the CCDID compared with continuous GDVN injection. This increased lattice hit rate can also be attributed to the separately prepared L1 sample used for CCDID (during beam time LW79) and GDVN (during beam time LV14) injections. These observations indicate that the droplet injection is capable of transporting intact crystals to the XFEL interaction region and that the sample droplets contain a crystal concentration comparable with that of the sample delivered with continuous GDVN injection. Another important observation was that the number of crystal lattices indexed was generally higher than the number of indexed patterns, indicating that multiple crystals were hit by an X-ray pulse during the experiments. This further supports a high crystal concentration in the droplets and no impact of the droplet generation on this quantity. The image analysis in Fig. 2, *B* and *C* further substantiates this finding, as crystals are imaged in similar proportions in generated droplets as in the sample solution transported through the inlet channel. In addition, Videos S1 and S2 demonstrate droplet generation with KDO8PS crystals with and without electrical triggering, respectively, and the transfer of multiple crystals into the droplets is evident.
3) The CCDID showed stable droplet generation with active feedback for durations of over 1 h for the three buffer systems tested, and in the L3 case (high viscosity buffer) droplet injection could be achieved for almost 4 h. In general, the time required by CCDID to obtain the same number of hits is longer compared with GDVN injections; however, during an SFX experiment this might not necessarily be a disadvantage. There is usually

a large number of experimental parameters that need to be optimized, including injection parameters (flow rate and gas pressures), detector calibration, and verification of data acquisition, before diffraction data collection can be successfully performed. These optimizations often require the use of the valuable sample for injection optimization. Thus, when the crystal sample amount is limited in amount or difficult to crystallize in large quantities, it may pose a challenge. CCDIDs can therefore be advantageous, as they can stretch the duration of a specific crystal sample volume to be used for experiment optimization and eventually overall data collection. Furthermore, XFEL down times or other infrastructure failures during an SFX experiment can lead to additional sample consumption, which can be minimized through droplet injection.

4) As reported in Table 1, the diffraction resolution for the three lysozyme preparations tested using both injection methods was found to range from 1.8 to 2.1 Å. In two of the three cases (L1 and L3 samples), the resolution was slightly better than with the continuous GDVN injection. This strongly supports that CCDIDs not only can prolong the sample usage during beam times but also indicates that droplet injection does not compromise the diffraction resolution.

A similar trend for higher crystal hits per sample volume consumed with CCDID was observed for KDO8PS crystals. The crystal hits per microliter for GDVN and for CCDID were 0.15 and 0.39, respectively, showing over 2-fold improvement for KDO8PS with CCDID compared with GDVN injection. However, the hit rate for the KDO8PS crystal sample was overall very low for both injection methods, not allowing a more detailed comparison in resolution. Since the composition of the KDO8PS sample solution differs from the lysozyme samples tested, this constitutes another example of the versatility of droplet injection through a CCDID.

Optimization strategies for droplet synchronization

The work presented here documents electrically stimulated droplet generation segmented with an immiscible oil for SFX and the reproducible injection of lysozyme and KDO8PS crystals, as well as diffraction data collection with this method. The implemented electrical feedback mechanism allows the adjustment of the phase delay of the droplet stimulation to account for a variable geometrical factor caused by the assembly procedure of the CCDIDs. We demonstrated the operating principle of this feedback mechanism; however, optimized synchronization to maximize droplet hit rate and, thus, crystal hit rate will be required in future applications of this novel injection method. The droplet hit rate is defined similarly to a crystal hit rate, indicating the fraction of droplets hit by the XFEL pulses. Since the droplet generation approach is based on continuous segmented oil and sample injection, detector images contain solution scattering information that can be used to diagnose the presence of fluorinated oil or sample solution in the path of the XFEL as detailed in materials and methods.

Fig. 6 shows an example of a data collection run in which improved droplet hit rate could be correlated with improved crystal hit rate. During the first 80 s droplets were generated with the CCDID without electrical stimulus, resulting in an average droplet hit rate of ≈17% and a corresponding average crystal hit rate of 0.14%. When the electrical feedback mechanism is turned on (*arrow* in Fig. 6), the average droplet hit rate increases to an average of ≈80% and, correspondingly, the average crystal hit rate increases to 1.58%. Thus, electrical stimulation with the implemented feedback mechanism resulted in 4-fold increase in droplet hit rate and a corresponding ≈10-fold increase in crystal hit rate. Fig. 6 further demonstrates that the droplet hit rate fluctuates (in two instances dropping to below 20%) during electrical stimulation. We relate this to instabilities of flow rates, which have been demonstrated

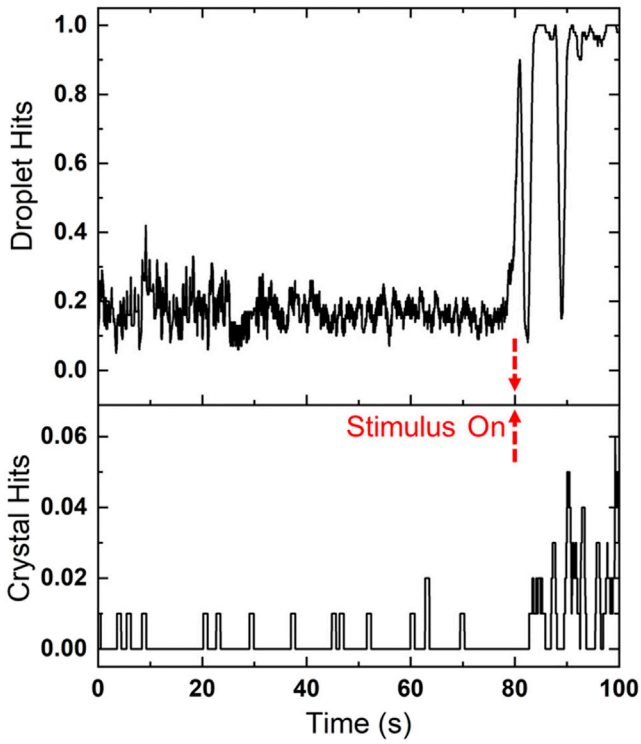

FIGURE 6 Snapshot of the droplet and crystal hit rates showing an increase in both rates upon application of electrical stimulation for lysozyme crystal sample (L2) during LV14.

to affect the stability of the droplet frequency in separate experiments (data not shown). To alleviate this issue, pumps with improved flow-rate control below 1 μL/min suitable for the high-pressure requirements of this liquid injection approach (up to ≈1000 psi) could be employed in future droplet injection experiments. Furthermore, the electrical feedback mechanism can be further improved to maximize the droplet hit rate using a systematic parameter sweep study. The limitations in time during the allocated MFX instrument experiments, however, did not allow for a more rigorous study of the droplet synchronization with the XFEL pulses but will be pursued in future SFX experiments.

CONCLUSION

We presented the implementation and characterization of CCDIDs for segmented droplet sample injection in serial crystallography experiments at the MFX instrument at LCLS for the first time with two protein crystal samples. The CCDID was composed of a 3D-printed droplet generator, optical droplet detector assembly, and a GDVN with a footprint small enough to be easily installed in the HERA chamber at the MFX instrument. A novel electrical triggering feedback mechanism was implemented successfully, allowing us to tune the droplet generation frequency of the CCDID at a programmed delay to the 120-Hz LCLS XFEL pulses. Droplet generation and stimulation over prolonged periods (>30 min) indicated immediate effects of applied electrical parameters on droplet generation frequency and phase delay to the XFEL pulses. A comparison between CCDID and continuous GDVN injection revealed a 4-fold increase in crystal hit rate per microliter injected with CCDID for lysozyme (L1) and KDO8PS crystal samples. Additionally, higher hit rates were observed for higher viscosity lysozyme samples (L2 and L3) compared with L1 for both injection methods, with GDVN injection showing slightly better performance. Diffraction resolution was similar between droplet and continuous injection for the lysozyme crystal samples tested, indicating excellent conservation of crystalline properties during electrically stimulated droplet injection. A real-time droplet hit rate analysis tool was also implemented, demonstrating the improvement of droplet and crystal hit rate with selected parameters as well as the possibility to optimize the droplet hit rate in future SFX experiments with XFELs employing the CCDID with electrical stimulation. However, the manual assembly procedures affecting geometric parameters of the CCDID (mainly the distance of droplet generation to the XFEL interaction region) and flow-rate instabilities require future characterization for improved synchronization of droplets with XFEL pulses. With the herein presented advances over previous nonstimulated droplet generation through a segmented flow approach (51), we further underline the ability of this emerging injection approach to improve one of the major bottlenecks in SFX with XFELs related to often prohibitively large sample consumption. Furthermore, the CCDIDs can be coupled to a mixing module upstream of the droplet generator in the future, and therefore offer a high potential for sample reduction in TR-SFX with XFELs.

SUPPORTING MATERIAL

Supporting material can be found online at https://doi.org/10.1016/j.bpr.2022.100081.

AUTHOR CONTRIBUTIONS

A.R. conceived the experiments. A.R., R.K., M.S., D.D., and A.E.G. designed the experiments. M.S., D.D., A.E.G., J.C.V., M.T.R., G.N., R.N., and A.R. contributed to device design and fabrication. A.E.G., D.D., J.C.V., and M.S. devised and fabricated the optical droplet detection setup. S.Z., K.K., R.A., and R.K. programmed the feedback mechanism. M.S., D.D., A.E.G., T.G., V.M., A.T., G.K., and S. Botha contributed to the various data analyses. P.F., A.M., S. Botha, D.D., D.T., H.H., R.B., J.M.M.-G., R.J., J.D.M.-A., and D.O. contributed to sample preparation. A.R., M.S., D.D., A.E.G., M.T.R., A.M., J.C.V., G.K., M.M., R.F., P.F., R.K., S. Botha, S.Z., G.N., R.K., J.M.M.-G., R.J., J.D.M.-A., and T.G. participated in the beamtime experiments either on-site or remotely. R.S., M.S.H., A.B., C.J.K., R.E.S., S.L., F.P., and S. Boutet contributed to instrument setup and experimental support, and participated as beamline scientists. M.S., A.R., A.E.G., and D.D. wrote the manuscript with input from all other co-authors.

ACKNOWLEDGMENTS

Financial support from the STC Program of the National Science Foundation through BioXFEL under agreement no. 1231306, NSF ABI Innovations award no. 1565180, and the National Institutes of Health award no. R01GM095583 is gratefully acknowledged. The use of the Linac Coherent Light Source (LCLS), SLAC National Accelerator Laboratory, is generously supported by the US Department of Energy, Office of Science, Office of Basic Energy Sciences under contract no. DE-AC02-76SF00515. The authors also thank the instrument group and facility staff for their assistance in the use of the MFX instrument during proposals MFXLV1418 and MFXLW7919 at LCLS. The HERA system for in-helium experiments at MFX was developed by Bruce Doak and funded by the Max Planck Institute for Medical Research. This work was also supported by The Center for Structural Dynamics in Biology, NIH grant P41GM139687.

DECLARATION OF INTERESTS

A.E.G., J.C.V., and A.R. hold a patent on electrical droplet stimulation in a 3D-printed device.

REFERENCES

1. Lee, J.-H., N. A. Zatsepin, and K. H. Kim. 2018. Time-resolved serial femtosecond X-ray crystallography. *BioDesign.* 6:15–22.

2. Wiedorn, M. O., D. Oberthur, …, A. Barty. 2018. Megahertz serial crystallography. *Nat. Commun.* 9:4025.
3. Fromme, P. 2015. XFELs open a new era in structural chemical biology. *Nat. Chem. Biol.* 11:895–899.
4. Johansson, L. C., B. Stauch, …, V. Cherezov. 2017. A Bright Future for Serial Femtosecond Crystallography with XFELs. *Trends Biochem. Sci.* 42:749–762.
5. Chapman, H. N., P. Fromme, …, J. C. Spence. 2011. Femtosecond X-ray protein nanocrystallography. *Nature.* 470:73–77.
6. Echelmeier, A., M. Sonker, and A. Ros. 2019. Microfluidic sample delivery for serial crystallography using XFELs. *Anal. Bioanal. Chem.* 411:6535–6547.
7. Neutze, R., R. Wouts, D. van der Spoel, E. Weckert, and J. Hajdu. 2000. Potential for biomolecular imaging with femtosecond X-ray pulses. *Nature.* 406:752–757.
8. Holmes, S., H. J. Kirkwood, …, C. Darmanin. 2022. Megahertz pulse trains enable multi-hit serial femtosecond crystallography experiments at X-ray free electron lasers. *Nat. Commun.* 13:4708.
9. Boutet, S., L. Lomb, …, I. Schlichting. 2012. High-resolution protein structure determination by serial femtosecond crystallography. *Science.* 337:362–364.
10. Boutet, S., and G. J Williams. 2010. The Coherent X-ray Imaging (CXI) instrument at the Linac Coherent Light Source (LCLS). *New J. Phys.* 12:035024.
11. Emma, P., R. Akre, …, J. Galayda. 2010. First lasing and operation of an ångstrom-wavelength free-electron laser. *Nat. Photonics.* 4:641–647.
12. Schlichting, I. 2015. Serial femtosecond crystallography: the first five years. *IUCrJ.* 2:246–255.
13. Ishchenko, A., C. Gati, and V. Cherezov. 2018. Structural biology of G protein-coupled receptors: new opportunities from XFELs and cryoEM. *Curr. Opin. Struct. Biol.* 51:44–52.
14. Stauch, B., and V. Cherezov. 2018. Serial Femtosecond Crystallography of G Protein-Coupled Receptors. *Annu. Rev. Biophys.* 47:377–397.
15. Liu, W., D. Wacker, …, V. Cherezov. 2013. Serial Femtosecond Crystallography of G Protein-Coupled Receptors. *Science.* 342:1521–1524.
16. Zhang, H., H. Unal, …, V. Cherezov. 2015. Structure of the Angiotensin Receptor Revealed by Serial Femtosecond Crystallography. *Cell.* 161:833–844.
17. Kang, Y., X. E. Zhou, …, H. E. Xu. 2015. Crystal structure of rhodopsin bound to arrestin by femtosecond X-ray laser. *Nature.* 523:561–567.
18. Gusach, A., I. Maslov, …, V. Cherezov. 2020. Beyond structure: emerging approaches to study GPCR dynamics. *Curr. Opin. Struct. Biol.* 63:18–25.
19. Lee, M.-Y., J. Geiger, …, W. Liu. 2020. Harnessing the power of an X-ray laser for serial crystallography of membrane proteins crystallized in lipidic cubic phase. *IUCrJ.* 7:976–984.
20. Fenalti, G., N. A. Zatsepin, …, V. Cherezov. 2015. Structural basis for bifunctional peptide recognition at human δ-opioid receptor. *Nat. Struct. Mol. Biol.* 22:265–268.
21. Grunbein, M. L., and G. Nass Kovacs. 2019. Sample delivery for serial crystallography at free-electron lasers and synchrotrons. *Acta Crystallogr D Struct Biol.* 75:178–191.
22. Stellato, F., D. Oberthur, …, H. N. Chapman. 2014. Room-temperature macromolecular serial crystallography using synchrotron radiation. *IUCrJ.* 1:204–212.
23. Garman, E. F., and M. Weik. 2017. Radiation Damage in Macromolecular Crystallography. *In* Protein Crystallography: Methods and Protocols. A. Wlodawer, Z. Dauter, and M. Jaskolski, eds. Springer New York, pp. 467–489.
24. Lomb, L., T. R. M. Barends, …, I. Schlichting. 2011. Radiation damage in protein serial femtosecond crystallography using an x-ray free-electron laser. *Phys. Rev. B.* 84:214111.
25. Spence, J. 2017. XFELs for structure and dynamics in biology. *IUCrJ.* 4:322–339.
26. Nam, K. H. 2020. Approach of Serial Crystallography. *Crystals.* 10:854.
27. Šrajer, V., and M. Schmidt. 2017. Watching proteins function with time-resolved x-ray crystallography. *J. Phys. Appl. Phys.* 50:373001.
28. Smith, J. L., R. F. Fischetti, and M. Yamamoto. 2012. Micro-crystallography comes of age. *Curr. Opin. Struct. Biol.* 22:602–612.
29. Schlichting, I., and J. Miao. 2012. Emerging opportunities in structural biology with X-ray free-electron lasers. *Curr. Opin. Struct. Biol.* 22:613–626.
30. Aquila, A., M. S. Hunter, …, H. N. Chapman. 2012. Time-resolved protein nanocrystallography using an X-ray free-electron laser. *Opt Express.* 20 (3):2706–2716.
31. Kupitz, C., S. Basu, …, P. Fromme. 2014. Serial time-resolved crystallography of photosystem II using a femtosecond X-ray laser. *Nature.* 513:261–265.
32. Kern, J., R. Tran, …, V. K. Yachandra. 2014. Taking snapshots of photosynthetic water oxidation using femtosecond X-ray diffraction and spectroscopy. *Nat. Commun.* 5:4371.
33. Young, I. D., M. Ibrahim, …, J. Yano. 2016. Structure of photosystem II and substrate binding at room temperature. *Nature.* 540:453–457.
34. Pandey, S., R. Bean, …, M. Schmidt. 2020. Time-resolved serial femtosecond crystallography at the European XFEL. *Nat. Methods.* 17:73–78.
35. Pande, K., C. D. Hutchison, …, M. Schmidt. 2016. Femtosecond structural dynamics drives the trans/cis isomerization in photoactive yellow protein. *Science.* 352:725–729.
36. Pandey, S., I. Poudyal, and T. N. Malla. 2020. Pump-Probe Time-Resolved Serial Femtosecond Crystallography at X-Ray Free Electron Lasers. *Crystals.* 10:628.
37. Nango, E., A. Royant, …, S. Iwata. 2016. A three-dimensional movie of structural changes in bacteriorhodopsin. *Science.* 354:1552–1557.
38. Nogly, P., T. Weinert, …, J. Standfuss. 2018. Retinal isomerization in bacteriorhodopsin captured by a femtosecond x-ray laser. *Science.* 361:eaat0094.
39. Claesson, E., W. Y. Wahlgren, …, S. Westenhoff. 2020. The primary structural photoresponse of phytochrome proteins captured by a femtosecond X-ray laser. *Elife.* 9:e53514.
40. Stagno, J. R., Y. Liu, …, Y. X. Wang. 2017. Structures of riboswitch RNA reaction states by mix-and-inject XFEL serial crystallography. *Nature.* 541:242–246.
41. Kupitz, C., J. L. Olmos, Jr., …, M. Schmidt. 2017. Structural enzymology using X-ray free electron lasers. *Struct Dyn.* 4:044003.
42. Weierstall, U., J. C. Spence, and R. B. Doak. 2012. Injector for scattering measurements on fully solvated biospecies. *Rev. Sci. Instrum.* 83:035108.
43. Nazari, R., S. Zaare, …, R. A. Kirian. 2020. 3D printing of gas-dynamic virtual nozzles and optical characterization of high-speed microjets. *Opt Express.* 28 (15):21749–21765.
44. Vakili, M., R. Vasireddi, …, M. Trebbin. 2020. Microfluidic polyimide gas dynamic virtual nozzles for serial crystallography. *Rev. Sci. Instrum.* 91:085108.
45. Hejazian, M., C. Darmanin, E. Balaur, and B. Abbey. 2020. Mixing and jetting analysis using continuous flow microfluidic sample delivery devices. *RSC Adv.* 10:15694–15701.
46. Chen, B., S. Kaledhonkar, …, J. Frank. 2015. Structural dynamics of ribosome subunit association studied by mixing-spraying

time-resolved cryogenic electron microscopy. *Structure.* 23:1097–1105.

47. Pandey, S., G. Calvey, …, M. Schmidt. 2021. Observation of substrate diffusion and ligand binding in enzyme crystals using high-repetition-rate mix-and-inject serial crystallography. *IUCrJ.* 8:878–895.
48. Oberthuer, D., J. Knoška, …, S. Bajt. 2017. Double-flow focused liquid injector for efficient serial femtosecond crystallography. *Sci. Rep.* 7:44628.
49. Calvey, G. D., A. M. Katz, …, L. Pollack. 2016. Mixing injector enables time-resolved crystallography with high hit rate at X-ray free electron lasers. *Struct Dyn.* 3:054301.
50. Hejazian, M., E. Balaur, and B. Abbey. 2021. Recent advances and future perspectives on microfluidic mix-and-jet sample delivery devices. *Micromachines-Basel.* 12:531.
51. Echelmeier, A., J. Cruz Villarreal, …, A. Ros. 2020. Segmented flow generator for serial crystallography at the European X-ray free electron laser. *Nat. Commun.* 11:4511.
52. Cheng, R. K. 2020. Towards an Optimal Sample Delivery Method for Serial Crystallography at XFEL. *Crystals.* 10:215.
53. Roedig, P., H. M. Ginn, …, A. Meents. 2017. High-speed fixed-target serial virus crystallography. *Nat. Methods.* 14:805–810.
54. Lahey-Rudolph, J. M., R. Schonherr, …, L. Redecke. 2021. Fixed-target serial femtosecond crystallography using in cellulo grown microcrystals. *IUCrJ.* 8:665–677.
55. Karpik, A., I. Martiel, …, C. Padeste. 2020. Fabrication of ultrathin suspended polymer membranes as supports for serial protein crystallography. *Micro and Nano Engineering.* 7:100053.
56. Doak, R. B., G. Nass Kovacs, …, I. Schlichting. 2018. Crystallography on a chip - without the chip: sheet-on-sheet sandwich. *Acta Crystallogr D Struct Biol.* 74:1000–1007.
57. Lyubimov, A. Y., T. D. Murray, …, J. M. Berger. 2015. Capture and X-ray diffraction studies of protein microcrystals in a microfluidic trap array. *Acta Crystallogr D Biol Crystallogr.* 71:928–940.
58. Denz, M., G. Brehm, …, S. Koster. 2017. Cyclic olefin copolymer as an X-ray compatible material for microfluidic devices. *Lab Chip.* 18:171–178.
59. Schieferstein, J. M., A. S. Pawate, …, P. J. A. Kenis. 2018. X-ray transparent microfluidic platforms for membrane protein crystallization with microseeds. *Lab Chip.* 18:944–954.
60. Hunter, M. S., B. Segelke, …, M. Frank. 2014. Fixed-target protein serial microcrystallography with an x-ray free electron laser. *Sci. Rep.* 4:6026.
61. Mueller, C., A. Marx, …, R. J. Dwayne Miller. 2015. Fixed target matrix for femtosecond time-resolved and in situ serial micro-crystallography. *Struct Dyn.* 2:054302.
62. Oghbaey, S., A. Sarracini, …, R. J. Miller. 2016. Fixed target combined with spectral mapping: approaching 100% hit rates for serial crystallography. *Acta Crystallogr D Struct Biol.* 72 (Pt 8):944–955.
63. Shelby, M. L., D. Gilbile, …, M. Frank. 2020. A fixed-target platform for serial femtosecond crystallography in a hydrated environment. *IUCrJ.* 7:30–41.
64. Lee, D., S. Park, …, J. Park. 2020. Application of a high-throughput microcrystal delivery system to serial femtosecond crystallography. *J. Appl. Crystallogr.* 53:477–485.
65. Weierstall, U., D. James, …, V. Cherezov. 2014. Lipidic cubic phase injector facilitates membrane protein serial femtosecond crystallography. *Nat. Commun.* 5:3309.
66. Liu, W., D. Wacker, …, V. Cherezov. 2014. Femtosecond crystallography of membrane proteins in the lipidic cubic phase. *Phil. Trans. Biol. Sci.* 369:20130314.
67. Sugahara, M., E. Mizohata, …, S. Iwata. 2014. Grease matrix as a versatile carrier of proteins for serial crystallography. *Nat. Methods.* 12:61.
68. Sugahara, M., C. Song, …, S. Iwata. 2016. Oil-free hyaluronic acid matrix for serial femtosecond crystallography. *Sci. Rep.* 6:24484.
69. Sierra, R. G., H. Laksmono, …, M. J. Bogan. 2012. Nanoflow electrospinning serial femtosecond crystallography. *Acta Crystallogr D Biol Crystallogr.* 68:1584–1587.
70. Sierra, R. G., C. Gati, …, H. DeMirci. 2016. Concentric-flow electrokinetic injector enables serial crystallography of ribosome and photosystem II. *Nat. Methods.* 13:59–62.
71. Jernigan, R., D. Logeswaran, and P. Fromme. 2022. Room temperature structural studies of sars cov-2 protein nendou with an x-ray free electron laser. *Structure*, In press.
72. Kim, D., A. Echelmeier, …, A. Ros. 2019. Electric Triggering for Enhanced Control of Droplet Generation. *Anal. Chem.* 91:9792–9799.
73. Echelmeier, A., D. Kim, …, A. Ros. 2019. 3D printed droplet generation devices for serial femtosecond crystallography enabled by surface coating. *J. Appl. Crystallogr.* 52:997–1008.
74. Mafune, F., K. Miyajima, …, M. Yabashi. 2016. Microcrystal delivery by pulsed liquid droplet for serial femtosecond crystallography. *Acta Crystallogr D Struct Biol.* 72:520–523.
75. Roessler, C. G., R. Agarwal, …, A. Zouni. 2016. Acoustic injectors for drop-on-demand serial femtosecond crystallography. *Structure.* 24:631–640.
76. Fuller, F. D., S. Gul, …, J. Yano. 2017. Drop-on-demand sample delivery for studying biocatalysts in action at X-ray free-electron lasers. *Nat. Methods.* 14:443–449.
77. Echelmeier, A., G. Nelson, …, A. Ros. 2015. Biphasic droplet-based sample delivery of protein crystals for serial femtosecond crystallography with an x-ray free electron laser. *MicroTAS - Int. Conf. Miniaturized Syst. Chem. Life Sci.* 19:1374–1376.
78. Boutet, S., A. E. Cohen, and S. Wakatsuki. 2016. The New Macromolecular Femtosecond Crystallography (MFX) Instrument at LCLS. *Synchrotron Radiat. News.* 29:23–28.
79. Sierra, R. G., A. Batyuk, …, S. Boutet. 2019. The Macromolecular Femtosecond Crystallography Instrument at the Linac Coherent Light SourceThis article will form part of a virtual special issue on X-ray free-electron lasers. *J. Synchrotron Radiat.* 26:346–357.
80. Wiedorn, M. O., S. Awel, …, H. N. Chapman. 2018. Rapid sample delivery for megahertz serial crystallography at X-ray FELs. *IUCrJ.* 5:574–584.
81. Han, H., E. Round, …, K. Lorenzen. 2021. The XBI BioLab for life science experiments at the European XFEL. *J. Appl. Crystallogr.* 54:7–21.
82. Conrad, C. E. 2016. Overcoming barriers in structural biology through method development of serial crystallography. Arizona State University.
83. Nelson, G., R. A. Kirian, …, M. Heymann. 2016. Three-dimensional-printed gas dynamic virtual nozzles for x-ray laser sample delivery. *Opt Express.* 24:11515–11530.
84. Lomb, L., J. Steinbrener, …, R. L. Shoeman. 2012. An anti-settling sample delivery instrument for serial femtosecond crystallography. *J. Appl. Crystallogr.* 45:674–678.
85. Van Rossum, G., and F. Drake. 2009. Python 3 reference manual createspace. Scotts Valley, CA.
86. Barty, A., R. A. Kirian, …, H. Chapman. 2014. Cheetah: software for high-throughput reduction and analysis of serial femtosecond X-ray diffraction data. *J. Appl. Crystallogr.* 47:1118–1131.
87. Mariani, V., A. Morgan, …, H. N. Chapman. 2016. OnDA: online data analysis and feedback for serial X-ray imaging. *J. Appl. Crystallogr.* 49 (Pt 3):1073–1080.
88. White, T. A., R. A. Kirian, …, H. N. Chapman. 2012. CrystFEL: a software suite for snapshot serial crystallography. *J. Appl. Crystallogr.* 45:335–341.

89. Gevorkov, Y., O. Yefanov, …, H. N. Chapman. 2019. XGANDALF - extended gradient descent algorithm for lattice finding. *Acta Crystallogr. A.* 75:694–704.

90. Powell, H. R., O. Johnson, and A. G. W. Leslie. 2013. Autoindexing diffraction images with iMosflm. *Acta Crystallogr. D.* 69:1195–1203.

91. Duisenberg, A. 1992. Indexing in single-crystal diffractometry with an obstinate list of reflections. *J. Appl. Crystallogr.* 25:92–96.

92. Doppler, D., M. T. Rabbani, …, A. Ros. 2022. Co-flow injection for serial crystallography at X-ray free-electron lasers. *J. Appl. Crystallogr.* 55:1–13.